



LaCo_{0.5}Ni_{0.5}O₃ perovskite for efficient sulfafurazole degradation via peroxyomonosulfate activation: Catalytic mechanism of interfacial structure

Zhuang He^{a,d,1}, Mengshan Chen^{b,1}, Ming Xu^{c,1}, Yingtang Zhou^b, Yunqiu Zhang^a, Guangzhi Hu^{a,*}

^a Southwest United Graduate School, School of Ecology and Environmental Science, Yunnan University, Kunming 650092, China

^b National Engineering Research Center for Marine Aquaculture, Marine Science and Technology College, Zhejiang Ocean University, Zhoushan 316004, China

^c State Key Laboratory of Chemical Resource Engineering, Beijing Advanced Innovation Center for Soft Matter Science and Engineering, Beijing University of Chemical Technology, Beijing 100029, China

^d School of Natural Resources and Environment, Northwest A&F University, Yangling, Shaanxi Province 712100, China



ARTICLE INFO

Keywords:

Peroxyomonosulfate
Organic pollutants
Catalytic degradation
Interface structure

ABSTRACT

This study reports the introduction of nickel species into the B-site metal center of LaCoO₃ perovskite, which shows high catalytic activity for sulfafurazole (SIZ) in solution by activating peroxyomonosulfate (PMS). A novel bimetallic lanthanum-based perovskite (LaCo_{0.5}Ni_{0.5}O₃) was designed by coprecipitation-calcination strategy, which can effectively degrade nearly 100% SIZ in 20 min by activating PMS. Density functional theory (DFT) calculations show that the interface structure of LaCo_{0.5}Ni_{0.5}O₃ has higher PMS adsorption capacity and faster electron transfer efficiency. Additionally, the interface structure of the B-site metal is more likely to promote PMS activation after the introduction of Ni species. Meanwhile, the Fukui index indicates the reaction sites of the active species attacking SIZ molecules and reasonably provides the possible degradation path of SIZ. This work provides an essential reference for the subsequent exploration of the catalytic mechanism of interfacial structure of heterogeneous catalysts based on PMS activation to degrade organic pollutants.

1. Introduction

With the rapid development of pharmaceuticals and medicines, antibiotics with extraordinary efficacy have been widely used to treat human and animal diseases [1]. However, the molecular structure of antimicrobial organics is complex, biodegradability is weak, and traditional pollutant treatment technology is challenging. If the pollutant treatment technology is improper and flows into the ecological environment (soil or water system) through various channels, it poses a potential threat to human health [2]. Among them, sulfonamides exposed to the ecological environment for a long time may promote biological toxicity, drug-resistant genes, and drug-resistant bacteria [3]. Additionally, some of the sulfonamide antibiotics (such as sulfamethoxazole, sulfafurazole, and sulfamethazine) have been recognized as carcinogenic by the International Agency for Research on Cancer (IARC) [4]. Therefore, there is an urgent to develop antibiotic organic pollutants treatment technologies with solid stability and excellent performance [5].

In recent years, various efficient breakthrough antibiotic wastewater treatment technologies have emerged with the continuous development in this field [6]. It is worth noting that the advanced oxidation processes (AOPs) based on activated peroxyomonosulfate (PMS) show unique advantages in the degradation of organic pollutants; therefore, they have been favored by researchers [7]. PMS produces oxidizing free radical species (SO₄[·] and OH) in the process of strong oxidative decomposition [8], or the singlet oxygen (1¹O₂) produced by PMS self-decomposition acts on the molecules of organic pollutants [9], thus giving rise to oxidative decomposition of organic pollutants and even mineralization into carbon dioxide and water or other small molecular substances [10]. However, among many PMS activation methods, the method based on transition metal catalysts has the advantages of low cost, simplicity, and high activation efficiency [11]. The heterogeneous catalytic activation method can effectively compensate for the loss of active metal sites and secondary pollution caused by the dissolution of metal ions during the homogeneous activation process and improve the catalytic efficiency of the reaction system [12]. Transition metal catalysts (Fe, Co, Mn) have

* Corresponding author.

E-mail address: guangzhihu@ynu.edu.cn (G. Hu).

¹ These authors contributed equally to this work.

been used in the heterogeneous catalytic activation of PMS, and their active substances (SO_4^{2-} , OH^- , and O_2) effectively degrade antibiotic organic pollutants in water. However, the overall catalytic efficiency of PMS oxidative decomposition still needs improvement [13].

Recently, perovskite-based oxides have been extensively studied in photoelectrochemistry and heterogeneous catalysis owing to their excellent chemical properties and high catalytic activity [14]. In the general chemical formula of perovskite (ABO_3), A is often regarded as a sizeable rare earth metal or alkali metal, and B represents a transition metal species [15]. LaCoO_3 perovskite oxide acts as an efficient activator of PMS and can effectively degrade organic pollutants in water [16]. However, the leaching of cobalt ions at the B site and the redox cycle of $\text{Co}^{3+}/\text{Co}^{2+}$ are limited, which seriously affects the catalytic activity of perovskite materials [13,17]. Studies have shown that the spatial configuration of the perovskite remains unchanged, with the introduction of oxygen vacancies, and the oxidation state of the B metal can be controlled by doping or introducing different foreign metal cations at the B site [18]. Lu et al. [19] found that $\text{LaCo}_{0.4}\text{Cu}_{0.6}\text{O}_3$ has a higher catalytic activity for removing phenolic organic compounds by introducing different metal cations (Fe, Cu, Mn) at the B-site structure of LaCoO_3 perovskite and promoting the $\text{Co}^{2+}/\text{Co}^{3+}$ redox cycling process by constructing a bimetallic system at the B-site. However, the reaction mechanism regulating the action of perovskite B metal cations for the activation of PMS is still unclear, and only the formation of catalytic reaction species and the performance optimization process are discussed [20]. A detailed explanation of the critical catalytic mechanism still needs clarification, such as highlighting the main activity center at the interface of perovskite materials doped or introduced with B-site metal cations, the mechanism by which the active centers activate PMS molecules, and the transfer of electrons at the interface between them [21]. Therefore, it is of great significance to study the interfacial structure's interaction and PMS activation mechanism after the introduction of B-site metal cations and to clarify the relationship between the active species and interfacial reaction sites of organic pollutants, which is of importance for the application of heterogeneous catalysts in the degradation of organic pollutants.

In this study, $\text{LaCo}_{0.5}\text{Ni}_{0.5}\text{O}_3$ perovskite materials were successfully prepared by a coprecipitation-high-temperature calcination method. We constructed a Fenton-like reaction system with PMS molecules, to explore the effect of introduction of B-site metal cations on the degradation of sulfafurazone (SIZ) in an aqueous environment by active center-activated PMS in perovskites. The physical and chemical properties of the $\text{LaCo}_{0.5}\text{Ni}_{0.5}\text{O}_3$ catalyst and the degradation of SIZ under different operating conditions were systematically investigated. The active center and interaction mechanism between $\text{LaCo}_{0.5}\text{Ni}_{0.5}\text{O}_3$ and the PMS molecular interface structure were further verified using density functional theory (DFT). Additionally, based on quenching experiments of active substances and electron paramagnetic resonance (EPR) analysis, the degradation mechanism of SIZ in the $\text{LaCo}_{0.5}\text{Ni}_{0.5}\text{O}_3/\text{PMS}$ system was proposed. In the DFT calculations, the Fukui index and liquid chromatography-mass spectrometry (LC-MS) confirmed the reaction sites and degradation intermediates of the interface structure of SIZ and provided the possible degradation pathway. This study provides an essential reference and theoretical basis for studying the mechanism of B-site element substitution in perovskite structures for PMS activation to remove persistent organic pollutants from water.

2. Materials and methods

2.1. Synthesis of $\text{LaCo}_{0.5}\text{Ni}_{0.5}\text{O}_3$

Details of the chemicals and reagents required for the preparation of the $\text{LaCo}_{0.5}\text{Ni}_{0.5}\text{O}_3$ catalysts are provided in Text S1. To prepare the catalysts, 0.4330 g of $\text{La}(\text{NO}_3)_3 \cdot 6\text{H}_2\text{O}$, 0.1455 g of $\text{Co}(\text{NO}_3)_2 \cdot 6\text{H}_2\text{O}$, and 0.1353 g of $\text{Ni}(\text{NO}_3)_2 \cdot 6\text{H}_2\text{O}$ (with a molar ratio of 1:0.5:0.5) were placed in a conical bottle containing 50 mL ultrapure water (labeled solution

A). After proper vibration and homogenization, solution A was ultrasonicated to fully dissolved it. Subsequently, the pre-configured 1 M NaOH solution was added to solution A until the pH of the mixed solution reached 12. In addition, the adjusted solution A was stirred by magnetic stirrer at 80 °C in a heat-collecting constant temperature oil bath for 2 h (rotational speed of 800 r min^{-1}). After cooling to room temperature (25 °C), the samples were filtered and washed three times with ultrapure water and anhydrous ethanol and then dried overnight in a blast dryer at 70 °C. Finally, the filter cake was ground to powder form and then placed in a tube furnace for 2 h for constant heat treatment at 800 °C at a heating rate of 3 °C min^{-1} . After cooling to room temperature, the $\text{LaCo}_{0.5}\text{Ni}_{0.5}\text{O}_3$ composite material was obtained. To determine the optimal molar ratio of Co to Ni species, LaCoO_3 , $\text{LaCo}_{0.7}\text{Ni}_{0.3}\text{O}_3$, $\text{LaCo}_{0.5}\text{Ni}_{0.5}\text{O}_3$, $\text{LaCo}_{0.3}\text{Ni}_{0.7}\text{O}_3$, $\text{LaCo}_{0.1}\text{Ni}_{0.9}\text{O}_3$, and LaNiO_3 composites were prepared according to the same preparation process. Additionally, the technical details related to the characterization of the composites in this work are provided in Text S2.

2.2. Experimental evaluation of $\text{LaCo}_{0.5}\text{Ni}_{0.5}\text{O}_3$ performance

The sulfonamide antibiotic sulfafurazone (SIZ) was used as a target pollutant to test the ability of $\text{LaCo}_{0.5}\text{Ni}_{0.5}\text{O}_3$ perovskite materials to catalyze the degradation of organic contaminants in the PMS environment. The degradation experiments for all catalysts were carried out in triplicate a 100 mL conical flask in triplicate. First, the pre-weighed composite material and an appropriate PMS activator were added to the conical bottle containing 50 mL of SIZ contaminant (10 mg L^{-1}). Subsequently, the conical flask was placed in a constant temperature oscillator at a temperature of 25 °C and a rotational speed of 150 r min^{-1} to react for 30 min. An appropriate amount of the reaction solution was taken out simultaneously and collected in a quartz colorimetric dish through a 0.45 μm organic needle filter. The concentration of the SIZ degraded solution after the reaction was measured using an ultraviolet-visible spectrophotometer (Genesys50, Thermo, USA) at a wavelength of 264 nm. The accurate concentrations of tetracycline, sulfamethoxazole, sulfamethazine, and chloramphenicol were determined at the optimal absorption wavelengths of 355, 264, 259 and 270 nm, respectively. The SIZ degraded pollutant concentration and reaction rate constant k can be calculated using Eq. S1 and S2 in the Supplementary information.

In the identification experiment of active species, ethanol (EtOH), tert-butanol (TBA), isopropanol (IPA) and L-histidine (L-his) were selected as effective quenchants to quench the corresponding active species in the reaction system further to clarify the primary and secondary effects of active species. All the catalysts in the cycle experiment were collected after the end of the degradation experiment, filtered and washed with ultra-pure water for 5 times.

2.3. Theoretical simulation methods

First-principles calculations were performed using the Vienna ab initio simulation package (VASP) using the generalized gradient approximation (GGA) and the Perdew-Burke-Ernzerhof (PBE) method based on density functional theory (DFT) [22]. The projector-augmented wave (PAW) describes the interaction between ions and electrons. The cut-off energy was set to 450 eV. A detailed calculation method and model structure were established as shown in Text S3.

3. Results and discussion

3.1. Characterization of the catalysts

The crystalline phase composition of the composites was determined by XRD analysis. As shown in Fig. 1a, the XRD patterns of LaCoO_3 and LaNiO_3 are in good agreement with standard diffraction patterns (JCPDS: 48-0123 and JCPDS: 34-1077), respectively [23]. The

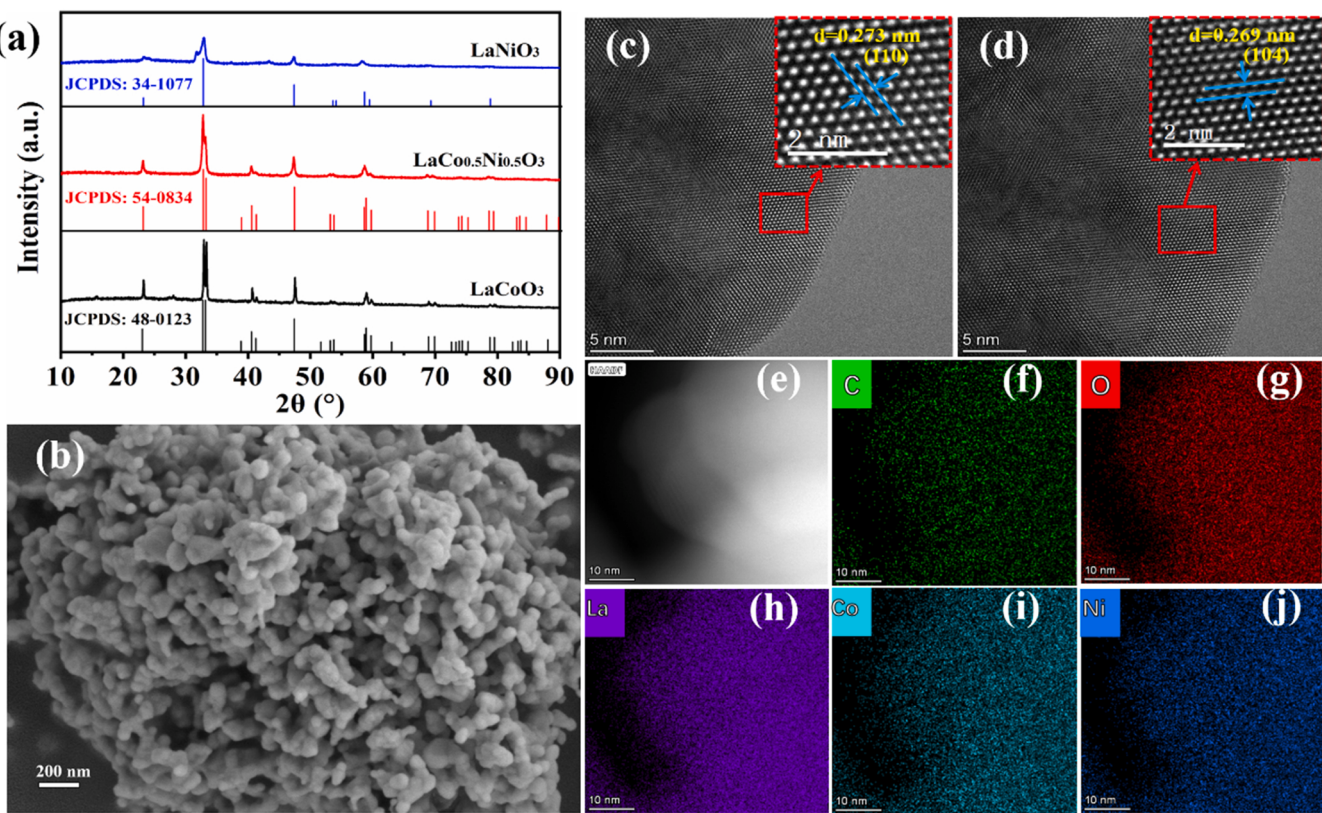


Fig. 1. (a) XRD patterns of LaCoO_3 , $\text{LaCo}_{0.5}\text{Ni}_{0.5}\text{O}_3$ and LaNiO_3 samples, (b) SEM images of $\text{LaCo}_{0.5}\text{Ni}_{0.5}\text{O}_3$ catalyst, (c)-(d) HAADF-STEM of $\text{LaCo}_{0.5}\text{Ni}_{0.5}\text{O}_3$ catalyst image, (e) Elemental mapping images of $\text{LaCo}_{0.5}\text{Ni}_{0.5}\text{O}_3$, (f)-(j) Elemental distribution on the surface of $\text{LaCo}_{0.5}\text{Ni}_{0.5}\text{O}_3$ catalyst.

$\text{LaCo}_{0.5}\text{Ni}_{0.5}\text{O}_3$ composite exhibited firm diffraction peaks, suggesting that the crystallinity of the catalyst was very high. The diffraction peaks at 23.1° , 32.7° , 33.2° , 40.5° , 47.3° , 58.5° , and 58.7° corresponding to the standard diffraction patterns of $\text{LaCo}_{0.5}\text{Ni}_{0.5}\text{O}_3$ at (012), (110), (104), (202), (024), (300), and (214), respectively. Interestingly, when adjusting the ratio of B-site cations to different transition metals, it was found that the diffraction peaks of different composites shifted slightly downward with the increasing Ni concentration, indicating that the substitution of Ni inhibited the production of large crystals (Fig. S1) [11]. However, the composites with different transition metal ratios still showed diffraction peaks matching those of the $\text{LaCo}_{0.5}\text{Ni}_{0.5}\text{O}_3$ perovskite, and no additional diffraction peaks appeared [24]. According to related literature, the downward shift of the diffraction peak may be attributed to the lattice deformation caused by the ion radius (0.061 nm) of Co being more significant than that of Ni (0.056 nm), which indicates that Ni was successfully introduced into the perovskite structure.

SEM and TEM characterizations were used to analyze the morphological structure of the $\text{LaCo}_{0.5}\text{Ni}_{0.5}\text{O}_3$ catalyst. As shown in Fig. 1b, $\text{LaCo}_{0.5}\text{Ni}_{0.5}\text{O}_3$ was composed of irregular aggregates, whereas nanoparticles condensed aggregates with a smooth and clear surface. The particle size was approximately 20–50 nm. Simultaneously, the irregular aggregate structure leaves abundant pore structures on its surface, which allows for the attachment of its pollutants on the surface of the $\text{LaCo}_{0.5}\text{Ni}_{0.5}\text{O}_3$ material and facilitates PMS activation [24]. Fig. S2a and S2b reveal the irregular nanoparticle morphology of the $\text{LaCo}_{0.5}\text{Ni}_{0.5}\text{O}_3$ catalysts, with highly uniform dispersions. Obvious lattice diffraction stripes were observed in the HRTEM images (Fig. S2c and S2d). After further characterization by HAADF-STEM (Fig. 1c and d), it was also observed that the lattice spacings of 0.273 nm and 0.269 nm corresponded to the lattice plane of $\text{LaCo}_{0.5}\text{Ni}_{0.5}\text{O}_3$ (JCPDS:54–0834), confirming the successful preparation of the $\text{LaCo}_{0.5}\text{Ni}_{0.5}\text{O}_3$ perovskite structure. Furthermore, STEM-EDS was used to reveal that the interfaces of $\text{LaCo}_{0.5}\text{Ni}_{0.5}\text{O}_3$ contained elements such as La, C, O, Co, and Ni.

Moreover, it can be seen from the elemental mapping (Fig. 1e-j), that Co and Ni are uniformly distributed on the surface, which is beneficial to promote the activation of PMS and participate in the degradation of SIZ pollutants.

X-ray absorption fine structure spectroscopy (XAFS) further identified the coordination environment and local atomic structure of $\text{LaCo}_{0.5}\text{Ni}_{0.5}\text{O}_3$. The Co K-edge X-ray absorption near-edge structure (XANES) spectra are shown in Fig. 2a. The energy absorption in $\text{LaCo}_{0.5}\text{Ni}_{0.5}\text{O}_3$ is between that of CoO and Co_2O_3 , which confirms that the valence state of Co is mainly the coexistence of +2 and +3. The pre-peak of $\text{LaCo}_{0.5}\text{Ni}_{0.5}\text{O}_3$ has a partial "overlap" behavior with Co_2O_3 at lower light energies, indicating that most are Co^{3+} ions [25]. The white line peak of $\text{LaCo}_{0.5}\text{Ni}_{0.5}\text{O}_3$ is much lower than that of the other comparators, which implies that the coordination environment and structural symmetry of $\text{LaCo}_{0.5}\text{Ni}_{0.5}\text{O}_3$ changed due to the introduction of Ni [26]. The XANES spectrum of the Ni K-edge (Fig. 2c) was similar to that of Co. In the near-edge region of low light energy, the Ni in $\text{LaCo}_{0.5}\text{Ni}_{0.5}\text{O}_3$ is very close to the NiO signal and Ni_2O_3 signal, implying that the valence state of Ni is also a coexistence state of +2 and +3. Additionally, the peak of the white line of $\text{LaCo}_{0.5}\text{Ni}_{0.5}\text{O}_3$ shifts to the low light energy of CoO , indicating that the Ni species in $\text{LaCo}_{0.5}\text{Ni}_{0.5}\text{O}_3$ show the characteristics of rich electrons and are easier to transform into high valence states [27]. In the Co K-edge extended X-ray photoelectron spectroscopy (EXAFS) spectrum of Fig. 2b, both $\text{LaCo}_{0.5}\text{Ni}_{0.5}\text{O}_3$ and Co_2O_3 show a strong peak at 1.4 Å, which is due to the contribution of the Co-O bond [28]. For the Ni K-edge (Fig. 2d), the strong peaks at 1.5, 2.5, 3.1, and 3.5 Å correspond to the Ni-O, Ni-Ni, Ni-La, and Ni-M bonds (M is Co or Ni), respectively [29]. The two-dimensional color patch image obtained by the EXAFS spectrum of the sample was obtained by wavelet transform, which further verified that the coordination environment of $\text{LaCo}_{0.5}\text{Ni}_{0.5}\text{O}_3$ was consistent with that obtained above, and Co-O, Co-M (La, Co, and Ni), Ni-O, and Ni-M (La, Co, and Ni) signals were detected (Fig. 2e-l). Additionally, XPS confirmed the interfacial

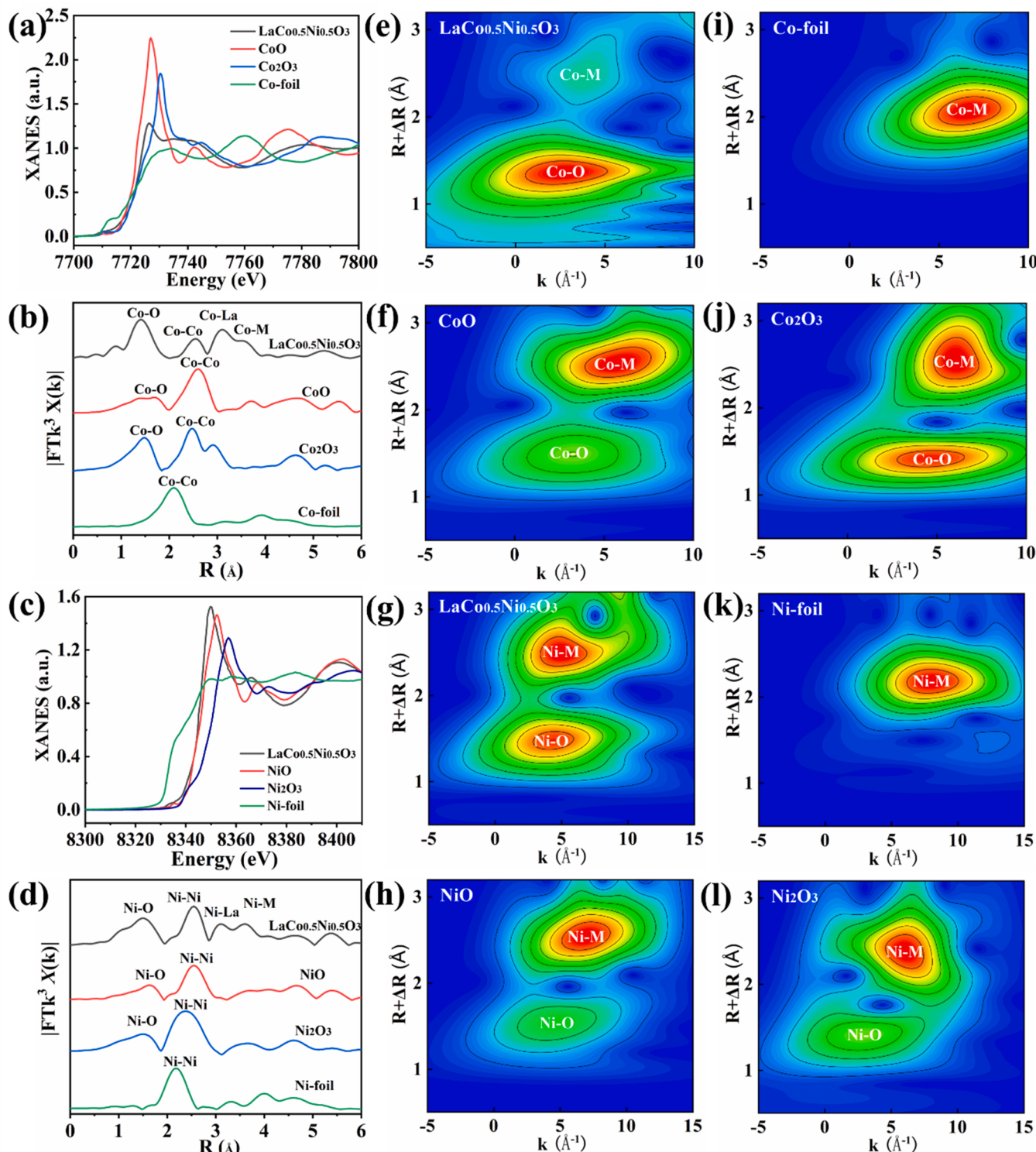


Fig. 2. (a) Co K-edge XANES spectrum, (b) Co K-edge EXAFS spectrum, (c) Ni K-edge XANES spectrum, (d) Ni K-edge EXAFS spectrum, (e)-(l) for the two-dimensional color block images obtained by wavelet transform of EXAFS spectra: (e) LaCo_{0.5}Ni_{0.5}O₃, (f) CoO, (g) LaCo_{0.5}Ni_{0.5}O₃, (h) NiO, (i) Co-foil, (j) Co₂O₃, (k) Ni-foil, (l) Ni₂O₃.

composition and elemental valence state of the LaCo_{0.5}Ni_{0.5}O₃ catalyst, as discussed in detail in Text S4.

3.2. Degradation performance of pollutants

The introduction of B-site cations changes the type and structure of perovskites, thereby affecting the catalytic performance of the materials.

Therefore, perovskite catalysts with different Co: Ni molar ratios were obtained by introducing the transition metal Ni into the perovskite structure to replace Co species on the B site, and the best ratio of perovskite catalysts was selected by activating PMS to degrade SIZ pollutants. Fig. S4 determines whether perovskite structures with different Co: Ni molar ratios can degrade SIZ pollutants. As shown in the figure, the SIZ removal efficiency of LaCoO₃, LaCo_{0.9}Ni_{0.1}O₃,

$\text{LaCo}_{0.7}\text{Ni}_{0.3}\text{O}_3$, $\text{LaCo}_{0.5}\text{Ni}_{0.5}\text{O}_3$, $\text{LaCo}_{0.3}\text{Ni}_{0.7}\text{O}_3$, $\text{LaCo}_{0.1}\text{Ni}_{0.9}\text{O}_3$, and LaNiO_3 catalysts in 30 min is 12.88%, 14.64%, 20.81%, 21.78%, 18.92%, 13.53% and 16.24%, respectively. The results show that the perovskite catalyst alone cannot effectively remove the SIZ pollutants. The degradation efficiency of the SIZ pollutants was significantly improved when an appropriate amount of PMS was introduced at different ratios of the perovskite systems. As shown in Fig. 3a, the degradation efficiencies of SIZ by LaCoO_3 , $\text{LaCo}_{0.9}\text{Ni}_{0.1}\text{O}_3$, $\text{LaCo}_{0.7}\text{Ni}_{0.3}\text{O}_3$, $\text{LaCo}_{0.5}\text{Ni}_{0.5}\text{O}_3$, $\text{LaCo}_{0.3}\text{Ni}_{0.7}\text{O}_3$, $\text{LaCo}_{0.1}\text{Ni}_{0.9}\text{O}_3$ and LaNiO_3 catalysts were improved to 98.97%, 99.02%, 99.11%, 98.88%, 98.43%, and 76.96%, respectively. Among them, $\text{LaCo}_{0.5}\text{Ni}_{0.5}\text{O}_3$ showed the highest catalytic activity with 99.30% degradation efficiency of SIZ within 20 min. In the kinetic exploration, it was found that the degradation process of SIZ followed quasi-primary reaction kinetics [30], corresponding to a better reaction rate than other perovskite catalysts with a constant k value of 0.2535 min^{-1} (Fig. 3b). Additionally, the utilization of PMS in the reaction system was explored to identify the best perovskite catalyst (Fig. 3c). The figure shows that the $\text{LaCo}_{0.5}\text{Ni}_{0.5}\text{O}_3$ and $\text{LaCo}_{0.9}\text{Ni}_{0.1}\text{O}_3$ catalysts have high PMS utilization rates (82.5% and 88.2%, respectively), indicating that their catalysts can effectively utilize PMS activation to generate active substances to participate in the degradation of SIZ pollutants. With a further increase in Ni introduction, the PMS utilization rate of gradually decreased. It is worth noting that when only PMS exists in the reaction system, the degradation rate of SIZ within 30 min is only 6.67%. The SIZ pollutants could hardly be degraded in the presence of PMS alone (Fig. 3d). In this work, the $\text{LaCo}_{0.5}\text{Ni}_{0.5}\text{O}_3$ catalyst has better catalytic activity with respect to degradation efficiency of SIZ, reaction kinetic constant k , and PMS utilization.

To identify the interface electron interaction mechanism behind the excellent effect of $\text{LaCo}_{0.5}\text{Ni}_{0.5}\text{O}_3$, the charge density distribution of the

material was investigated using the Bader charge method in DFT calculations [31]. Fig. 4a-c analyzes the projected density of states (PDOS) of the LaCoO_3 , LaNiO_3 , and $\text{LaCo}_{0.5}\text{Ni}_{0.5}\text{O}_3$ samples. It can be observed from the figure that with the introduction of Ni, the d-band centers of Co and Ni decrease in $\text{LaCo}_{0.5}\text{Ni}_{0.5}\text{O}_3$, and the decline of Co species is significantly more than that of Ni species, indicating that Co species in $\text{LaCo}_{0.5}\text{Ni}_{0.5}\text{O}_3$ have a greater probability of 3d electron transition than Ni. Therefore, in the process of catalytic degradation of SIZ, $\text{LaCo}_{0.5}\text{Ni}_{0.5}\text{O}_3$ is more available to provide electrons for PMS than LaCoO_3 and the LaNiO_3 matrix; that is, $\text{LaCo}_{0.5}\text{Ni}_{0.5}\text{O}_3$ has better catalytic activity. Furthermore, the performance of the above catalysts with different ratios was confirmed. It is worth noting that in the calculated PDOS diagram, the values of the d-band center of La in LaCoO_3 , LaNiO_3 and $\text{LaCo}_{0.5}\text{Ni}_{0.5}\text{O}_3$ are 0.551 eV, 0.894 eV and 0.747 eV, respectively. This means that the d-band center of $\text{LaCo}_{0.5}\text{Ni}_{0.5}\text{O}_3$ is higher than that of LaCoO_3 but lower than that of LaNiO_3 . Therefore, the La atoms in $\text{LaCo}_{0.5}\text{Ni}_{0.5}\text{O}_3$ effectively regulate the adsorption and desorption energy barriers of Co and Ni atoms on the catalyst surface, thereby improving their catalytic activity. Additionally, the Co species in $\text{LaCo}_{0.5}\text{Ni}_{0.5}\text{O}_3$ may provide electrons more easily than Ni atoms. Follow-up work further demonstrated the primary and secondary interactions of Co and Ni atoms in $\text{LaCo}_{0.5}\text{Ni}_{0.5}\text{O}_3$.

3.3. Effects of inorganic anions and applicability of the system

In the $\text{LaCo}_{0.5}\text{Ni}_{0.5}\text{O}_3$ /PMS system, the amount of catalyst, PMS, and solution pH were closely related to SIZ degradation. The control variable method was used to explore the effects of different factors on the SIZ degradation and PMS activation. The detailed discussion is presented in Supplementary information Text S5. SIZ pollutants have a wide

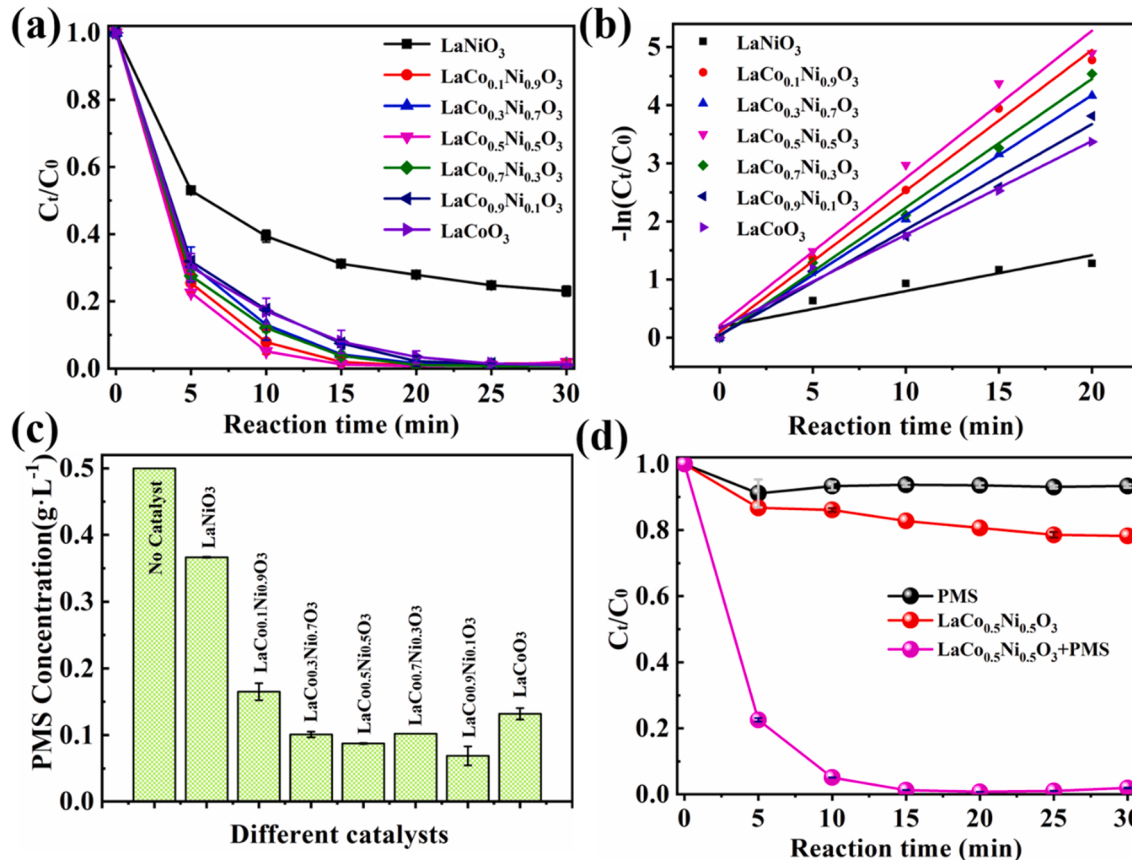


Fig. 3. (a) Effect of different metal ratios on the degradation efficiency of SIZ, (b) Reaction rates of activated PMS with different B-site metal ratios, (c) The residual concentration of PMS in different metal ratio systems, (d) Performance experiments. [Catalyst] = 0.2 g L^{-1} , [PMS] = 0.812 mM , [SIZ concentration] = 10 mg L^{-1} .

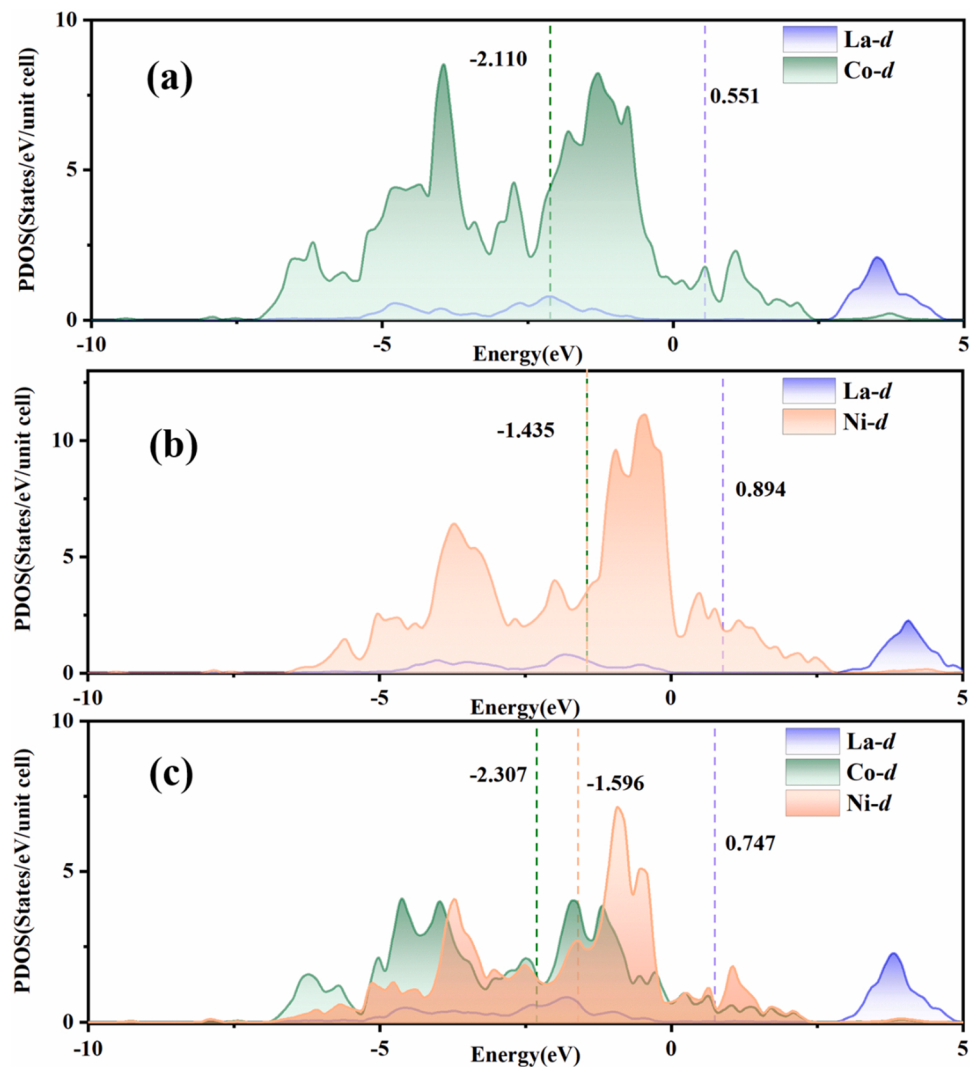


Fig. 4. (a), (b) and (c) correspond to the optimized configurations of PDOS for LaCoO_3 , LaNiO_3 and $\text{LaCo}_{0.5}\text{Ni}_{0.5}\text{O}_3$ samples, respectively.

application range in a solution pH of 5–9, in $\text{LaCo}_{0.5}\text{Ni}_{0.5}\text{O}_3/\text{PMS}$ systems. However, there are many types of inorganic anions (Cl^- , HCO_3^- , H_2PO_4^- , NO_3^-) in the natural water matrix, which may affect the degradation of SIZ pollutants by the $\text{LaCo}_{0.5}\text{Ni}_{0.5}\text{O}_3/\text{PMS}$ system. Therefore, this study focuses on the effects of four typical inorganic anions (with the same concentration of 10 mM) on the degradation of SIZ pollutants. As shown in Fig. 5a, the introduction of 10 mM of Cl^- , $\text{LaCo}_{0.5}\text{Ni}_{0.5}\text{O}_3/\text{PMS}$ into the system inhibited the degradation of the target pollutant (SIZ), and the degradation rate of SIZ by $\text{LaCo}_{0.5}\text{Ni}_{0.5}\text{O}_3/\text{PMS}$ in 30 min was 60.25%. This may be because Cl^- in the reaction system reacts with active species (SO_4^{2-} and OH) to produce free radical species with weak oxidation abilities (HClO , $\text{Cl}\cdot$, and $\text{Cl}_2\cdot$) [32]. Interestingly, when 10 mM HCO_3^- was introduced into the reaction system, SIZ was significantly inhibited at the initial stage of the reaction, and the SIZ degradation rate after 30 min was only 36.01%. This phenomenon at the initial stage of the reaction is attributed to the chemical properties of HCO_3^- itself, which will lead to a rapid increase in the pH of the solution and inhibition of the interaction between the reaction systems. At the same time, the introduction of HCO_3^- will also react with the active species in the reaction system to produce free radical species with relatively weak oxidation abilities ($\text{HCO}_3\cdot$ and $\text{CO}_3\cdot$) [33]. The introduction of H_2PO_4^- and NO_3^- reduced the removal efficiency of SIZ pollutants, but the degradation rate of the overall target pollutants (SIZ) was still excellent, with degradation rates of 96.40% and 93.72%, respectively.

Tetracycline (TC), sulfamethoxazole (SMX), sulfamethazine (SMT), and chloramphenicol (CAP) were selected as target pollutants to verify the universal applicability of the $\text{LaCo}_{0.5}\text{Ni}_{0.5}\text{O}_3/\text{PMS}$ system in the degradation of different organic pollutants. As shown in Fig. S6a, the $\text{LaCo}_{0.5}\text{Ni}_{0.5}\text{O}_3/\text{PMS}$ system could degrade TC pollutants in water for approximately 20 min. However, the SMX, SMT and CAP degradation effects were not as good as those of the former, and the corresponding degradation rates after 30 min were 93.12% and 96.39%, respectively. However, the $\text{LaCo}_{0.5}\text{Ni}_{0.5}\text{O}_3/\text{PMS}$ system could achieve a degradation rate of more than 86% for the above-mentioned typical organic antibiotic compounds. This shows that the $\text{LaCo}_{0.5}\text{Ni}_{0.5}\text{O}_3$ perovskite material has potential for constructing a Fenton-like system to remove organic pollutants from water. A cycle experiment was used to determine the reuse and stability of the $\text{LaCo}_{0.5}\text{Ni}_{0.5}\text{O}_3$ catalyst. The recovered catalyst was placed under the optimum reaction conditions in advance, and after four cycles of experiments, the $\text{LaCo}_{0.5}\text{Ni}_{0.5}\text{O}_3/\text{PMS}$ reaction system still exhibited a degradation rate of more than 90% of SIZ in water (Fig. 5b). To clarify the reason for the decrease of the catalytic effect of $\text{LaCo}_{0.5}\text{Ni}_{0.5}\text{O}_3$ in the cycle experiment, the leaching amount of cobalt metal ions after degradation was determined to be 2.74 mg L^{-1} by ICP-OES analysis technology. Therefore, the weakening of the catalytic effect of cyclic experiments may be attributed to the partial leaching of cobalt metal active sites in $\text{LaCo}_{0.5}\text{Ni}_{0.5}\text{O}_3$ materials. In addition, some residual small molecules on the surface of the material

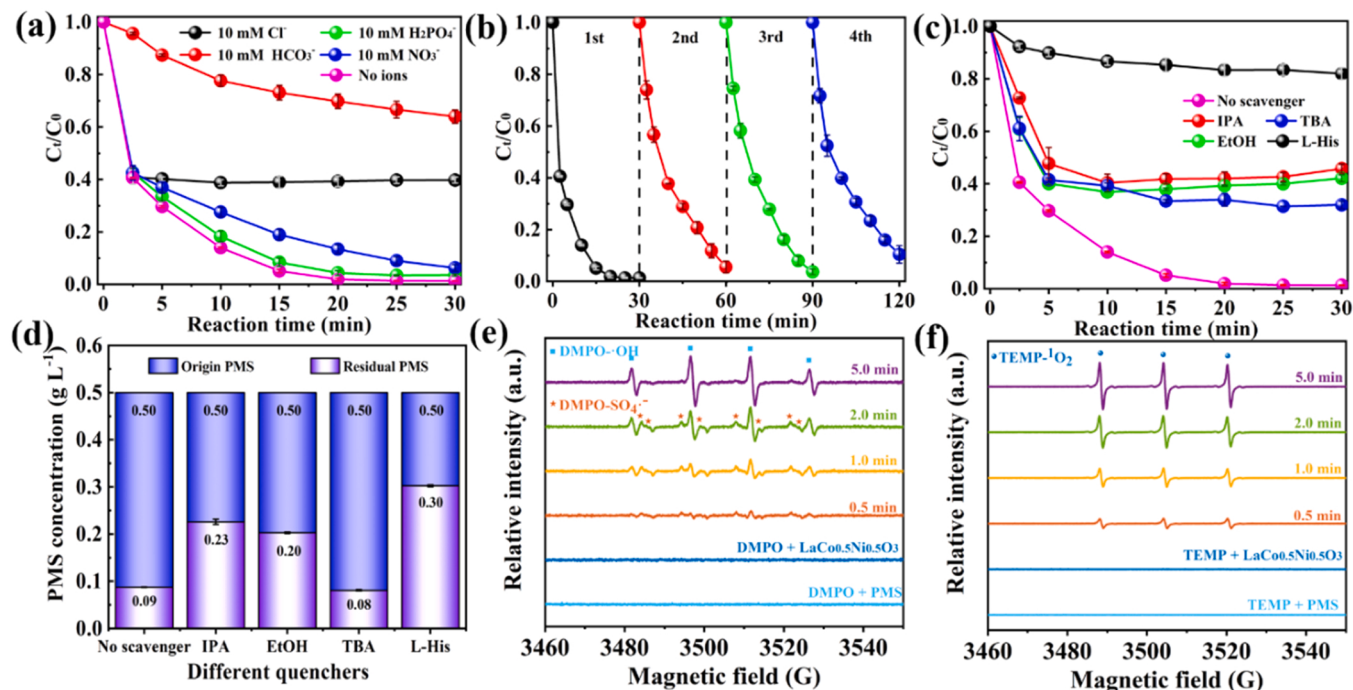


Fig. 5. (a) Effect of inorganic anions, (b) Recycling of $\text{LaCo}_{0.5}\text{Ni}_{0.5}\text{O}_3$ catalysts, (c) Active species capture experiments, (d) Effect of different capture agents on PMS activation. (e) EPR spectrum of DMPO as a spin trap, (f) EPR spectrum of TEMP as a spin trap. Reaction conditions: $[\text{LaCo}_{0.5}\text{Ni}_{0.5}\text{O}_3] = 0.2 \text{ g L}^{-1}$, $[\text{PMS}] = 0.812 \text{ mM}$, [SIZ concentration] = 10 mg L^{-1} .

will mask the active site, resulting in the weakening of its catalytic effect.

3.4. Identification of active species

To identify the active species produced by the $\text{LaCo}_{0.5}\text{Ni}_{0.5}\text{O}_3/\text{PMS}$ system, four quenchers were selected to determine the primary and secondary roles of the active species in the system. EtOH has been reported to effectively quench SO_4^2- and $\cdot\text{OH}$ species in the reaction system. In contrast, TBA mainly quenched the $\cdot\text{OH}$ species in the system [34]. Additionally, the high affinity of IPA owing to its low dielectric constant can simultaneously quench free radicals and free radical species on the catalyst surface [35]. As shown in Fig. 5c, the introduction of EtOH, TBA, and IPA caused the $\text{LaCo}_{0.5}\text{Ni}_{0.5}\text{O}_3/\text{PMS}$ system to inhibit SIZ degradation to varying degrees, with corresponding degradation efficiencies of 57.92%, 68.06%, and 54.26%, respectively. The reaction rate constants k were 0.0191, 0.0300, and 0.0203 min⁻¹, respectively (Fig. S6b). This phenomenon indicates that active species, such as SO_4^2- and $\cdot\text{OH}$, are involved in the degradation of SIZ in the $\text{LaCo}_{0.5}\text{Ni}_{0.5}\text{O}_3/\text{PMS}$ system. The inhibitory effect of EtOH was greater than that of TBA, indicating that SO_4^2- may play a dominant role in the degradation of the SIZ reaction system. Notably, the IPA quencher showed a slightly more substantial inhibitory effect than EtOH, implying that the free radicals on the surface of $\text{LaCo}_{0.5}\text{Ni}_{0.5}\text{O}_3$ also promoted SIZ degradation [11]. Moreover, L-his is often used to quench $^1\text{O}_2$ in the reaction system. It can be observed from the figure that the introduction of L-his dramatically slows down the degradation efficiency of the SIZ. The degradation rate after 30 min was only 18.02% ($k = 0.0054 \text{ min}^{-1}$). This indicates a non-radical process of $^1\text{O}_2$ in the reaction system and plays a leading role in the degradation of SIZ. The PMS decomposition efficiency in the capture experiment was explored to understand the quenching mechanism of the $\text{LaCo}_{0.5}\text{Ni}_{0.5}\text{O}_3/\text{PMS}$ system. As shown in Fig. 5d, the addition of EtOH, IPA, and L-his to the reaction system as quenchers may slow the contact of the $\text{LaCo}_{0.5}\text{Ni}_{0.5}\text{O}_3$ catalyst with PMS, thereby inhibiting the decomposition of PMS. The introduction of TBA may consume free radical species in the reaction system, thereby

accelerating the activation process of PMS. Thus, the remaining PMS concentration is lowered.

The EPR experiment was used to determine the active species produced by the $\text{LaCo}_{0.5}\text{Ni}_{0.5}\text{O}_3/\text{PMS}$ system. Fig. 5e shows that no active species signal peak was observed in the initial reaction stage in the $\text{DMPO} + \text{LaCo}_{0.5}\text{Ni}_{0.5}\text{O}_3$ and $\text{DMPO} + \text{PMS}$ systems. However, when the $\text{LaCo}_{0.5}\text{Ni}_{0.5}\text{O}_3$ catalyst coexists with PMS, the signal peak of $\text{DMPO}-\text{SO}_4^2-$ can be observed in the reaction after 1 min. As the reaction continued for up to 5 min, a $\text{DMPO}-\text{OH}$ signal peak with a 1:2:2:1 ratio appeared, mainly because the SO_4^2- in the system reacted with the OH^- in the solution to further produce $\cdot\text{OH}$. TEMP is often used as a spin trap for $^1\text{O}_2$ [36]. As shown in Fig. 5f, the same results as those in Fig. 3e were obtained for the $\text{LaCo}_{0.5}\text{Ni}_{0.5}\text{O}_3$ catalyst alone or in the system containing only PMS, where no signal peak of the active species appeared. A $\text{TEMP}-^1\text{O}_2$ weak signal peak with an intensity ratio of 1:1:1 appeared at the initial stage of the reaction system (0.5 min). Moreover, as the reaction system proceeded for 5 min, the intensity of the $\text{TEMP}-^1\text{O}_2$ signal peak increased significantly, which is attributed to the fact that the self-decomposition of PMS in the reaction system also promotes the production of $^1\text{O}_2$. Therefore, the EPR analysis techniques verified the existence of three active species in the $\text{LaCo}_{0.5}\text{Ni}_{0.5}\text{O}_3/\text{PMS}$ system.

3.5. Mechanism exploration of $\text{LaCo}_{0.5}\text{Ni}_{0.5}\text{O}_3/\text{PMS}$ system

The influence of ionic strength can determine the interfacial reaction type of heterogeneous catalysis [11]. Among them, the increase in ionic strength hinders the electrostatic interaction between the material surfaces, that is, the outer spherical interaction. If the reaction system is an inner spherical interaction, it will not be affected [37,38]. Therefore, different concentrations of NaClO_4 were added to the optimal reaction system to further explore the interfacial reaction between $\text{LaCo}_{0.5}\text{Ni}_{0.5}\text{O}_3$ and PMS. As shown in Fig. 6a, in the system containing NaClO_4 , the degradation rate of SIZ was not significantly affected or even slightly improved, indicating that the primary type of interfacial reaction between $\text{LaCo}_{0.5}\text{Ni}_{0.5}\text{O}_3$ and PMS may be the inner-sphere interaction mechanism. In other words, there is a strong binding or complex

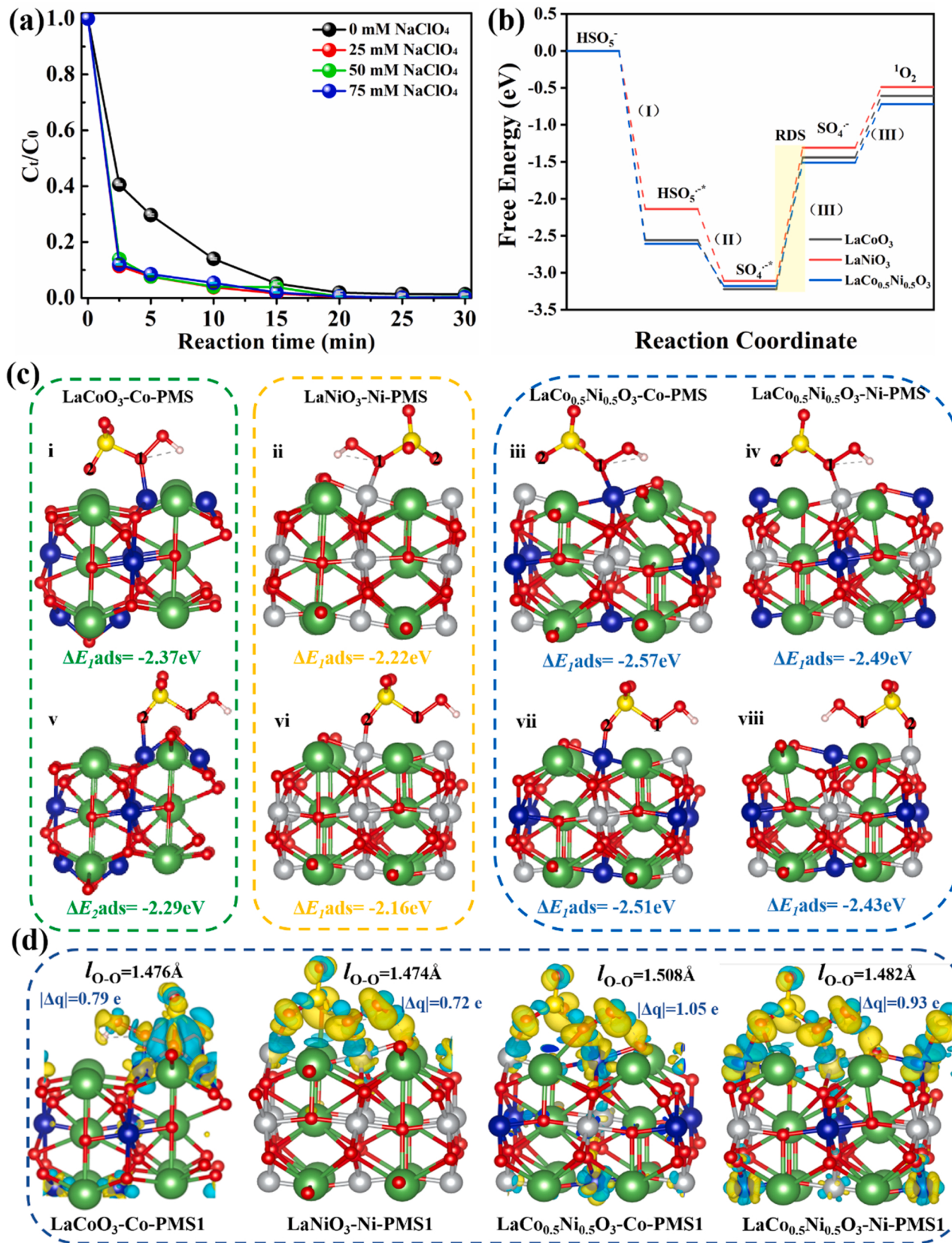


Fig. 6. (a) Effect of different concentrations of NaClO_4 on the reaction system, (b) Calculated free energy of three samples for the PMS to $^1\text{O}_2$ process, (c) The possible adsorption configurations of PMS on the metal active centers of different samples (i and v - LaCoO_3 , ii and vi: LaNiO_3 , iii, iv, vii and viii: $\text{LaCo}_{0.5}\text{Ni}_{0.5}\text{O}_3$), (d) Interface electron density difference diagrams of LaCoO_3 , LaNiO_3 , $\text{LaCo}_{0.5}\text{Ni}_{0.5}\text{O}_3$ and PMS. Dark green, blue, gray, red, yellow and white represent La, Co, Ni, O, S and H, respectively.

relationship between the metal active sites in the $\text{LaCo}_{0.5}\text{Ni}_{0.5}\text{O}_3$ catalyst and PMS, which promotes the activation of PMS to produce active species for SIZ degradation.

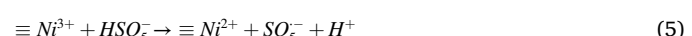
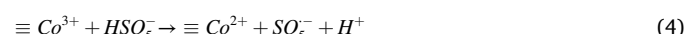
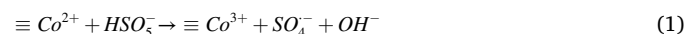
To reveal the adsorption and activation mechanism of PMS at the sample interface, the adsorption energies of PMS at the molecular level on LaCoO_3 , LaNiO_3 and $\text{LaCo}_{0.5}\text{Ni}_{0.5}\text{O}_3$ catalysts were calculated and analyzed by DFT. In AOPs technology involving PMS, the metal center is often a PMS active site [28]. Higher activities of Co and Ni atoms in the catalytic system were observed in the PDOS of the above samples. Therefore, this work mainly analyzes the adsorption energy changes of two types of O atoms of PMS (Type I is a peroxy O atom ($\text{O}1$) and Type II is a terminal O atom ($\text{O}2$)) on Co and Ni sites of the sample [39]. As shown in Fig. 6c, the adsorption energies of PMS at the interface of the LaCoO_3 , LaNiO_3 , and $\text{LaCo}_{0.5}\text{Ni}_{0.5}\text{O}_3$ catalysts are all negative ($\Delta E_{\text{ads}} < 0$), which means that the adsorption process of PMS on the sample interface is favorable. Notably, the adsorption energy of the Co or Ni sites at the interface between the $\text{O}1$ end and LaCoO_3 , LaNiO_3 , and $\text{LaCo}_{0.5}\text{Ni}_{0.5}\text{O}_3$ samples was more negative than that at the $\text{O}2$ end (Fig. 6c (i)-(viii)), indicating that the adsorption type between PMS and the samples was mainly dominated by the $\text{O}1$ end, which was more likely to form a stable adsorption conformation. The adsorption energy of PMS at the Co site decreased from -2.37 eV to -2.57 eV in LaCoO_3 due to the introduction of Ni atoms in the $\text{LaCo}_{0.5}\text{Ni}_{0.5}\text{O}_3$ catalyst. This indicates that the introduction of Ni atoms strengthens the strong adsorption binding between the metal active sites on the $\text{LaCo}_{0.5}\text{Ni}_{0.5}\text{O}_3$ interface and PMS, which confirms the conjecture of the ionic strength experiment. Additionally, the adsorption configuration ($\Delta E_{\text{ads}} = -2.57$ eV) of the Co site at the interface between PMS and $\text{LaCo}_{0.5}\text{Ni}_{0.5}\text{O}_3$ has a higher adsorption energy than that of the Ni site ($\Delta E_{\text{ads}} = -2.49$ eV). Therefore, PMS is more likely to be first adsorbed on the Co site at the interface of $\text{LaCo}_{0.5}\text{Ni}_{0.5}\text{O}_3$, promoting its activation to produce reactive oxygen species that act on the degradation of SIZ pollutants.

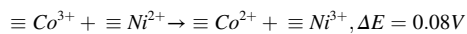
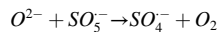
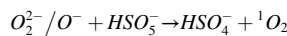
The Gibbs free energy (ΔG) provides direct evidence of the PMS activation mechanism in the catalytic system (Fig. 6b) [40]. Pathway (I) in the figure shows that $\text{LaCo}_{0.5}\text{Ni}_{0.5}\text{O}_3$ ($\Delta E_{\text{ads}} = -2.61$ eV) has the lowest energy barrier for adsorption compared to LaCoO_3 ($\Delta E_{\text{ads}} = -2.56$ eV) and LaNiO_3 ($\Delta E_{\text{ads}} = -2.14$ eV), indicating a higher catalytic activity of $\text{LaCo}_{0.5}\text{Ni}_{0.5}\text{O}_3$, which agrees with the above results. In the dissociation process of HSO_5^- (pathway (II)), we found that the dissociation energy of $\text{LaCo}_{0.5}\text{Ni}_{0.5}\text{O}_3$ ($\Delta E_{\text{dis}} = -0.57$ eV) was lower than that of LaCoO_3 ($\Delta E_{\text{dis}} = -0.66$ eV) and LaNiO_3 ($\Delta E_{\text{dis}} = -0.97$ eV), which revealed that the interfacial $\text{LaCo}_{0.5}\text{Ni}_{0.5}\text{O}_3$ structure was more favorable for the transfer of electrons to HSO_5^- during the dissociation of PMS molecules [41]. The formation of $\text{SO}_4^{\cdot-}$ is a potential rate-determining step (RDS) for LaCoO_3 , LaNiO_3 and $\text{LaCo}_{0.5}\text{Ni}_{0.5}\text{O}_3$. It can be seen that pathway (III) $\text{LaCo}_{0.5}\text{Ni}_{0.5}\text{O}_3$ shows the lowest energy barrier in the RDS (1.67 eV). Moreover, the desorption energy of $\text{LaCo}_{0.5}\text{Ni}_{0.5}\text{O}_3$ ($\Delta E_{\text{des}} = 0.79$ eV) was much lower than that of LaCoO_3 ($\Delta E_{\text{des}} = 0.83$ eV) and LaNiO_3 ($\Delta E_{\text{des}} = 0.82$ eV) during the $\text{SO}_4^{\cdot-}$ desorption conversion to ${}^1\text{O}_2$. Thus, the lower reaction energy barriers for the desorption process of RDS and $\text{SO}_4^{\cdot-}$ further demonstrate that $\text{LaCo}_{0.5}\text{Ni}_{0.5}\text{O}_3$ is more favorable for promoting PMS activation and is more likely to produce active species ($\text{SO}_4^{\cdot-}$ and ${}^1\text{O}_2$) for the pollutant degradation reaction.

To elucidate the primary and secondary roles of PMS activation by Co and Ni metal sites at the material interface, the variation in the transferred charges of LaCoO_3 , LaNiO_3 , and $\text{LaCo}_{0.5}\text{Ni}_{0.5}\text{O}_3$ were further explored. As shown in Fig. 6d, the cyan area represents charge depletion in the sample, and the yellow area represents the charge accumulation in the sample. In contrast, in the formation of the $\text{LaCo}_{0.5}\text{Ni}_{0.5}\text{O}_3$ material, electron redistribution occurred at the interface [31]. The electron transfer quantities of LaCoO_3 -Co-PMS1 and LaCoO_3 -Ni-PMS1 calculated by Bader topology are 0.79e and 0.72e, respectively. After transition metals are introduction at B, the number of electrons transferred from the Ni sites on the $\text{LaCo}_{0.5}\text{Ni}_{0.5}\text{O}_3$ interface to the PMS is approximately

0.93e, while the number of electrons transferred from the Co metal sites to the PMS reaches 1.05e. The higher electron transfer amount indicates that holes accumulate in Co atoms more than in Ni atoms, which promotes the adsorption of electronegative PMS on the Co sites of the $\text{LaCo}_{0.5}\text{Ni}_{0.5}\text{O}_3$ interface structure to generate active species, which is consistent with the results shown in Fig. 4a. Additionally, Fig. 6d shows that the O–O bond (lo–o) in the molecular structure of PMS extended from the original 1.451–1.508 Å upon Co binding at the $\text{LaCo}_{0.5}\text{Ni}_{0.5}\text{O}_3$ interface. The Lo–o of the other samples after binding is significantly less than 1.508 Å, which indicates a higher activity of the PMS molecules after the binding of Co with PMS at the $\text{LaCo}_{0.5}\text{Ni}_{0.5}\text{O}_3$ interface, which is more conducive for the decomposition into active species involved in the degradation of SIZ pollutants [41].

Additionally, the fresh and used $\text{LaCo}_{0.5}\text{Ni}_{0.5}\text{O}_3$ materials were compared using XPS analysis to further clarify the PMS activation mechanism. The detailed analytical procedure is presented in Text S6. Based on the above research results, the catalytic mechanism of $\text{LaCo}_{0.5}\text{Ni}_{0.5}\text{O}_3$ catalyst activating PMS was proposed. As shown in Fig. 4c, the active sites of the $\text{LaCo}_{0.5}\text{Ni}_{0.5}\text{O}_3$ catalysts Co^{2+} and Ni^{2+} directly activate PMS molecules adsorbed on the material surface to produce the active species $\text{SO}_4^{\cdot-}$ and $\cdot\text{OH}$ (Eqs. (1–3)). In addition, the detailed DFT calculations explained in detail the interaction mechanism between the active metal sites and PMS molecules, and confirmed that the contribution of Co species to the activation of PMS molecules was more significant than that of Ni. Simultaneously, the standard redox potentials of $\text{Co}^{3+}/\text{Co}^{2+}$ and $\text{Ni}^{3+}/\text{Ni}^{2+}$ were higher than those of the $\text{HSO}_5^-/\text{SO}_5^-$ species [42]. Therefore, Co^{3+} and Ni^{3+} can react with HSO_5^- molecules to produce Co^{2+} and Ni^{2+} , which promotes the decomposition of PMS molecules and produce other active species (Eqs. (4) and (5)). The C=O group in the $\text{LaCo}_{0.5}\text{Ni}_{0.5}\text{O}_3$ catalyst material and the rich electron transfer process at the interface facilitated the self-decomposition of PMS molecules, resulting in a non-free radical mechanism ${}^1\text{O}_2$ (Eqs. (6)–(8)) [43]. It is essential that the surface-dissociated oxygen ($\text{O}_2^{\cdot-}/\text{O}'$) adsorbs PMS molecules on the surface of the $\text{LaCo}_{0.5}\text{Ni}_{0.5}\text{O}_3$ catalyst to produce the active material ${}^1\text{O}_2$ (Eq. (9)) [44]. In addition, the lattice oxygen (O^{2-}) on the surface of the $\text{LaCo}_{0.5}\text{Ni}_{0.5}\text{O}_3$ catalyst reacted with the active species SO_5^- generated during the oxidative decomposition of PMS molecules to produce $\text{SO}_4^{\cdot-}$ (Eq. (10)) [45], which enhanced the degradation of SIZ organic pollutants. This further validates the reason for the decrease in the intensity of the O^{2-} and $\text{O}_2^{\cdot-}/\text{O}'$ accessory peaks in the O 1 s XPS spectra before and after the reaction. Combined with the above active substance quenching experiments and EPR analysis results, it is found that the non-radical mechanism ${}^1\text{O}_2$ plays a vital role in the degradation of SIZ pollutants. Furthermore, the standard redox potential of the B-site metal cation $\text{Co}^{3+}/\text{Co}^{2+}$ (1.92 V) in the $\text{LaCo}_{0.5}\text{Ni}_{0.5}\text{O}_3$ catalyst, is higher than that of $\text{Ni}^{3+}/\text{Ni}^{2+}$ (1.84 V). Therefore, Ni^{2+} is thermodynamically favorable for the reduction of Co^{3+} to Co^{2+} (Eq. (11)), which will effectively improve the cycle process of $\text{Co}^{3+}/\text{Co}^{2+}$ and then promotes the oxidative decomposition of PMS to remove SIZ pollutants from water.





3.6. Possible degradation pathways

DFT calculations further revealed the vulnerable reaction sites of the active species during SIZ degradation (Fig. 7a) [46]. Simultaneously, the highest occupied orbital (HOMO) and the lowest unoccupied orbital

(9)

(10)

(11)

(LUMO) of the SIZ pollutants provide sites prone to electron escape and electron acceptance, respectively (Fig. 7b and c). 1O_2 , SO_4^- , and ${}^{\cdot}OH$ all have strong electrophilicity and are more likely to attack the position of the escaping electrons in the molecular structure of SIZ. As shown in Fig. 7b, the HOMO of the molecular structure of SIZ was mainly concentrated in the aniline, isoxazole, and S-N bonds. The Fukui index (f-) calculated using DFT was used to further analyze the positions of SIZ molecules vulnerable to electrophilic attacks [27]. Fig. 7d shows the relatively high Fukui indices of C1 (f-=0.070), C5 (f-=0.067), C6 (f-=0.080), C10 (f-=0.090), N17 (f-=0.072), O13 (f-=0.054) and S15 (f-=0.056), indicating that these atomic positions are vulnerable to

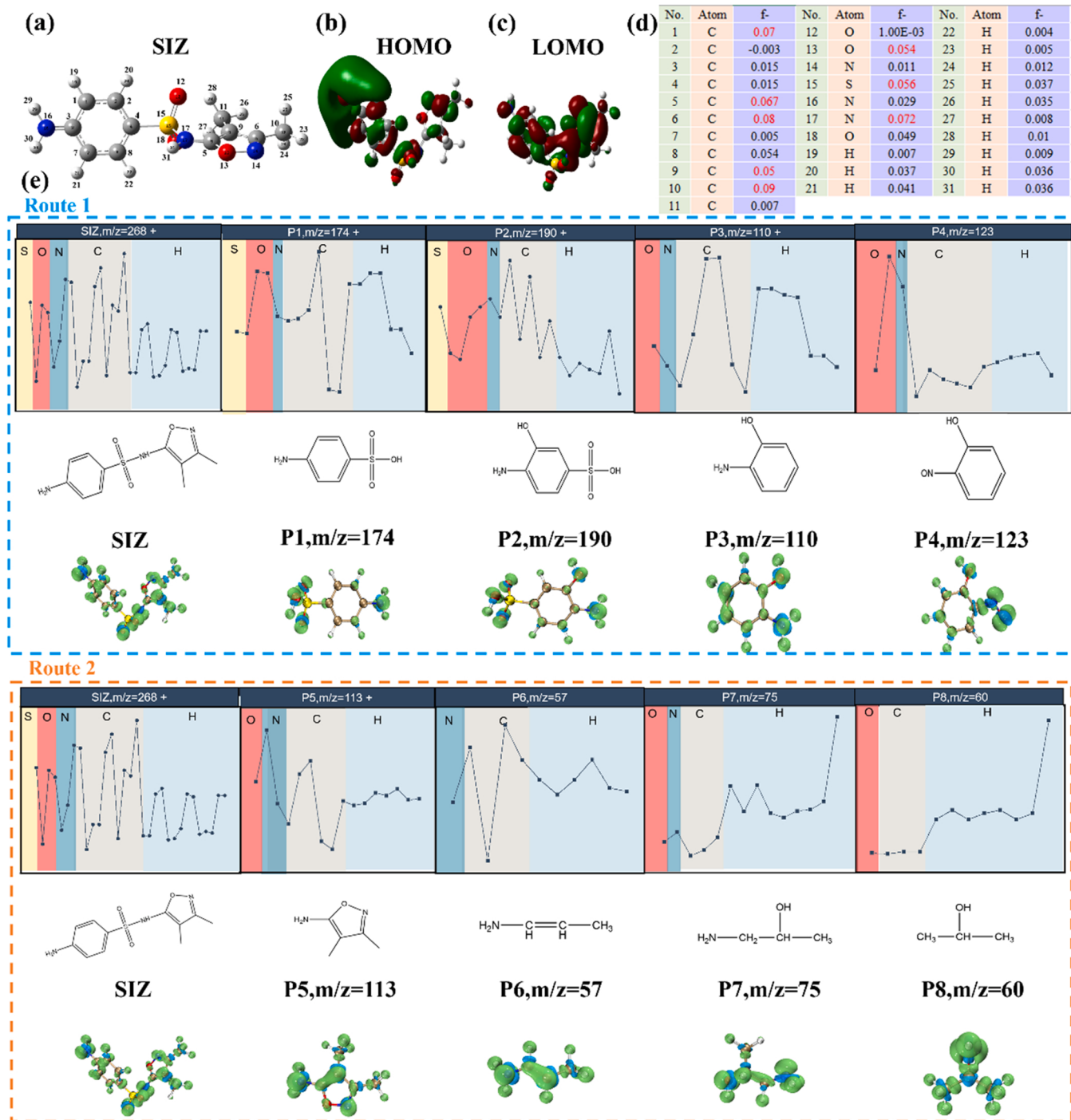


Fig. 7. (a) Chemical structure of SIZ, (b) HOMO diagram of SIZ, (c) LOMO diagram of SIZ, (d) Fukui index corresponding to each atom in the structure of SIZ, (e) The possible degradation routes of SIZ.

attack by living species. The Fukui index and LC-MS were used to analyze the intermediate products of SIZ degradation. The specific results for the SIZ degradation intermediates are listed in Table S1. In Path 1 of Fig. 7e, the S-N bond connected between the aniline and the oxazole parts cleaves under the attack of the active species to form P1 ($m/z = 174$), corresponding to the higher Fukui index of N17 ($f=0.072$) [47]. C1 on the aniline in P1 was hydroxylated by $^1\text{O}_2$, SO_4^- , and OH to produce P2 ($m/z = 190$) [48]. Then, the continuous oxidation of active species then promotes the cleavage of the C-S bond to form P3 ($m/z = 110$), and the -NH_2 bond connected to the benzene ring in P3 undergoes nitrosation to form P4 ($m/z = 123$). In Path 2, an oxidation process similar to Path 1 (cleavage of the S-N bond) occurred, resulting in the intermediate product P5 ($m/z = 113$). The active species attacked the C6 and O13 active sites in the P5 structure to form P6 ($m/z = 57$). Subsequently, small-molecular compounds P7 ($m/z = 75$) and P8 ($m/z = 60$) were formed by further oxidation. In path 3 (Fig. S8), P9 ($m/z = 156$), and P10 ($m/z = 94$) compounds were also oxidized by the S-N bond and C-S bonds, respectively. In Path 4, the highly active site of C10 ($f=0.090$) was broken to form P11 ($m/z = 254$) under the attack by the active species. Subsequently, the C-N bond was broken by $^1\text{O}_2$, SO_4^- , and OH to form a P12 ($m/z = 173$) compound, which is consistent with the higher Fukui index of C5 ($f=0.067$) and N17 ($f=0.072$). Finally, the intermediate products from the SIZ degradation are mineralized to CO_2 and H_2O under the continuous oxidation conditions of the active species. Therefore, the Fukui index in the DFT calculation reveals the degradation path of the SIZ more intuitively and accurately, which providing a new approach for analyzing the degradation path of pollutants in the future.

To evaluate the toxicity level of intermediates produced by SIZ degradation, the acute and chronic toxicities of SIZ and its intermediates were predicted using ECOSAR software (Table S2) [49]. A consistent toxicity level classification method (Globally Harmonized System of Classification and Labeling of Chemicals (GHS)) was compared with the SIZ. In terms of acute toxicity, SIZ is harmful to the survival of water fleas and green algae, but harmless to fish. The LC50 and EC50 values of most of the intermediates produced increase in acute toxicity, among which P1, P2, P7, and P8 intermediates were harmless. Regarding chronic toxicity, it was found that the water flea was the most sensitive to SIZ and its intermediates. Among them, a small number of intermediates (P3, P9, P10, P11, and P12) were highly toxic to water fleas, whereas the toxicity of products degraded further in the active species was weakened. The bioaccumulation factors and developmental toxicity of SIZ and its intermediates were analyzed using toxicity assessment software (T.E.S.T) (Fig. S9). Fig. S9 shows that most intermediate bioaccumulation factors and developmental toxicity were significantly reduced in the $\text{LaCo}_{0.5}\text{Ni}_{0.5}\text{O}_3/\text{PMS}$ system, indicating a decrease in the ability of intermediates to accumulate and develop toxicity *in vivo* [50]. Additionally, the mineralization effect of the SIZ pollutants in the reaction system was analyzed using Total Organic Carbon (TOC). After 30 min of treatments, the SIZ mineralization rate of the $\text{LaCo}_{0.5}\text{Ni}_{0.5}\text{O}_3/\text{PMS}$ system reached 53%, revealing that the system degraded SIZ pollutants into intermediates and then further mineralized them into CO_2 , H_2O , and low molecular substances, which significantly reduces harm to the water environment.

4. Conclusions

In summary, $\text{LaCo}_{0.5}\text{Ni}_{0.5}\text{O}_3$ was successfully prepared by introducing the B-site metal center of LaCoO_3 perovskite into Ni species through a simple coprecipitation-high temperature calcination process, which can catalyze the degradation of SIZ pollutants after activating PMS molecules. DFT calculations showed that the active interfacial unit of the $\text{LaCo}_{0.5}\text{Ni}_{0.5}\text{O}_3$ catalyst had a strong binding affinity with the PMS molecule. The difference in charge density, change in interfacial electron transfer and free energy further revealed the internal degradation mechanism of the $\text{LaCo}_{0.5}\text{Ni}_{0.5}\text{O}_3$ catalyst promoting the reaction system

and determined that the Co species in the B-site bimetallic active unit contributed more to the activation of PMS molecules. Additionally, the reaction sites and intermediates of the structural degradation of SIZ were accurately analyzed and combined with ECOSAR and T.E.S.T software, and it was observed that the biotoxicity of the intermediates decreased significantly. Therefore, combined with basic experiments and DFT calculations, this work describes in detail the degradation mechanism and reaction pathway of organic pollutants in a Fenton-like heterogeneous system, which not only solves the difficulties in the discussion of the catalytic mechanism but also provides a theoretical basis and scientific support for the subsequent removal of organic pollutants.

CRediT authorship contribution statement

Zhuang He: Conceptualization, Validation, Investigation, Resources, Data curation, Writing – original draft, Visualization. **Mengshan Chen:** Resources, Software, Validation, Visualization. **Ming Xu:** Resources, Software, Visualization. **Yingtang Zhou:** Validation, Investigation, Software, Visualization, Writing – review & editing. **Yunqiu Zhang:** Investigation, Software, Visualization. **Guangzhi Hu:** Resources, Writing – review & editing, Supervision, Project administration, Funding acquisition.

Declaration of Competing Interest

The authors declare that they have no known competing financial interests or personal relationships that could have appeared to influence the work reported in this paper.

Data Availability

Data will be made available on request.

Acknowledgments

This work was financially supported by National Key Research and Development Program of China (2019YFC1804400), the Special Project for Social Development of Yunnan Province (202103AC100001), and Double First-Class University Plan (C176220100042). The authors thank the Advanced Analysis and Measurement Center of Yunnan University for the sample testing service.

Appendix A. Supporting information

Supplementary data associated with this article can be found in the online version at [doi:10.1016/j.apcatb.2023.122883](https://doi.org/10.1016/j.apcatb.2023.122883).

References

- [1] G. Boczkaj, A. Fernandes, Wastewater treatment by means of advanced oxidation processes at basic pH conditions: a review, *Chem. Eng. J.* 320 (2017) 608–633.
- [2] I.T. Carvalho, L. Santos, Antibiotics in the aquatic environments: a review of the European scenario, *Environ. Int.* 94 (2016) 736–757.
- [3] K. Kümmerer, Antibiotics in the aquatic environment – a review – Part II, *Chemosphere* 75 (2009) 435–441.
- [4] C. Yan, Y. Yang, J. Zhou, M. Liu, M. Nie, H. Shi, L. Gu, Antibiotics in the surface water of the Yangtze Estuary: occurrence, distribution and risk assessment, *Environ. Pollut.* 175 (2013) 22–29.
- [5] Q.Q. Zhang, G.G. Ying, C.G. Pan, Y.S. Liu, J.L. Zhao, Comprehensive evaluation of antibiotics emission and fate in the river basins of China: source analysis, multimedia modeling, and linkage to bacterial resistance, *Environ. Sci. Technol.* 49 (2015) 6772–6782.
- [6] R. Xu, Z.-H. Yang, Q.-P. Wang, Y. Bai, J.-B. Liu, Y. Zheng, Y.-R. Zhang, W.-P. Xiong, K. Ahmad, C.-Z. Fan, Rapid startup of thermophilic anaerobic digester to remove tetracycline and sulfonamides resistance genes from sewage sludge, *Sci. Total Environ.* 612 (2018) 788–798.
- [7] D. Wu, P. Ye, M. Wang, Y. Wei, X. Li, A. Xu, Cobalt nanoparticles encapsulated in nitrogen-rich carbon nanotubes as efficient catalysts for organic pollutants degradation via sulfite activation, *J. Hazard. Mater.* 352 (2018) 148–156.

[8] M. Xu, J. Li, Y. Yan, X. Zhao, J. Yan, Y. Zhang, B. Lai, X. Chen, L. Song, Catalytic degradation of sulfamethoxazole through peroxymonosulfate activated with expanded graphite loaded CoFe_2O_4 particles, *Chem. Eng. J.* 369 (2019) 403–413.

[9] S. Zhu, X. Li, J. Kang, X. Duan, S. Wang, Persulfate activation on crystallographic manganese oxides: mechanism of singlet oxygen evolution for nonradical selective degradation of aqueous contaminants, *Environ. Sci. Technol.* 53 (2019) 307–315.

[10] Q. Yang, Y. Ma, F. Chen, F. Yao, J. Sun, S. Wang, K. Yi, L. Hou, X. Li, D. Wang, Recent advances in photo-activated sulfate radical-advanced oxidation process (SR-AOP) for refractory organic pollutants removal in water, *Chem. Eng. J.* 378 (2019).

[11] C. Cheng, S. Gao, J. Zhu, G. Wang, L. Wang, X. Xia, Enhanced performance of LaFeO_3 perovskite for peroxymonosulfate activation through strontium doping towards 2,4-D degradation, *Chem. Eng. J.* 384 (2020), 123377.

[12] S. Rodriguez, L. Vasquez, D. Costa, A. Romero, A. Santos, Oxidation of orange G by persulfate activated by Fe(II), Fe(III) and zero valent iron (ZVI), *Chemosphere* 101 (2014) 86–92.

[13] K.-Y.A. Lin, Y.-C. Chen, Y.-F. Lin, LaMO_3 perovskites (M=Co, Cu, Fe and Ni) as heterogeneous catalysts for activating peroxymonosulfate in water, *Chem. Eng. Sci.* 160 (2017) 96–105.

[14] J. Simböck, M. Ghiasi, S. Schönebaum, U. Simon, F.M.F. de Groot, R. Palkovits, Electronic parameters in cobalt-based perovskite-type oxides as descriptors for chemocatalytic reactions, *Nat. Commun.* 11 (2020) 652.

[15] J. Suntivich, K.J. May, H.A. Gasteiger, J.B. Goodenough, Y. Shao-Horn, A. Perovskite, Oxide optimized for oxygen evolution catalysis from molecular orbital principles, *Science* 334 (2011) 1383–1385.

[16] X. Pang, Y. Guo, Y. Zhang, B. Xu, F. Qi, LaCoO_3 perovskite oxide activation of peroxymonosulfate for aqueous 2-phenyl-5-sulfobenzimidazole degradation: Effect of synthetic method and the reaction mechanism, *Chem. Eng. J.* 304 (2016) 897–907.

[17] O.P. Taran, A.B. Ayusheev, O.L. Ogorodnikova, I.P. Prosvirin, L.A. Isupova, V. N. Parmon, Perovskite-like catalysts LaBO_3 (B=Ca, Fe, Mn, Co, Ni) for wet peroxide oxidation of phenol, *Appl. Catal. B: Environ.* 180 (2016) 86–93.

[18] H. Zhu, P. Zhang, S. Dai, Recent advances of lanthanum-based perovskite oxides for catalysis, *ACS Catal.* 5 (2015) 6370–6385.

[19] S. Lu, G. Wang, S. Chen, H. Yu, F. Ye, X. Quan, Heterogeneous activation of peroxymonosulfate by $\text{LaCo}_{1-x}\text{Cu}_x\text{O}_3$ perovskites for degradation of organic pollutants, *J. Hazard. Mater.* 353 (2018) 401–409.

[20] P. Gao, S. Yan, X. Tian, Y. Nie, Y. Wang, Y. Deng, J. Tu, Identification and manipulation of active centers on perovskites to enhance catalysis of peroxymonosulfate for degradation of emerging pollutants in water, *J. Hazard. Mater.* 424 (2022), 127384.

[21] X. Duan, C. Su, J. Miao, Y. Zhong, Z. Shao, S. Wang, H. Sun, Insights into perovskite-catalyzed peroxymonosulfate activation: maneuverable cobalt sites for promoted evolution of sulfate radicals, *Appl. Catal. B Environ.* 220 (2018) 626–634.

[22] G. Kresse, J. Furthmüller, Efficient iterative schemes for ab initio total-energy calculations using a plane-wave basis set, *Phys. Rev. B* 54 (1996) 11169–11186.

[23] Q. Pan, Q. Gao, G. Gao, M. Liu, B. Han, K. Xia, C. Zhou, Composition-engineered LaCoO_3 -based monolithic catalysts for easily operational and robust peroxymonosulfate activation, *Chem. Eng. J.* 424 (2021), 130574.

[24] P. Liang, D. Meng, Y. Liang, Z. Wang, C. Zhang, S. Wang, Z. Zhang, Cation deficiency tuned $\text{LaCoO}_{3-\delta}$ perovskite for peroxymonosulfate activation towards bisphenol A degradation, *Chem. Eng. J.* 409 (2021), 128196.

[25] M.M. Arman, N.G. Imam, R. Loredo Portales, S.I. El-Dek, Synchrotron radiation X-ray absorption fine structure and magnetization improvement of A-site Ce³⁺-doped LaFeO_3 , *J. Magn. Magn. Mater.* 513 (2020), 167097.

[26] Y. Hou, M. Qiu, M.G. Kim, P. Liu, G. Nam, T. Zhang, X. Zhuang, B. Yang, J. Cho, M. Chen, C. Yuan, L. Lei, X. Feng, Atomically dispersed nickel–nitrogen–sulfur species anchored on porous carbon nanosheets for efficient water oxidation, *Nat. Commun.* 10 (2019) 1392.

[27] J. Qi, X. Yang, P.-Y. Pan, T. Huang, X. Yang, C.-C. Wang, W. Liu, Interface engineering of Co(OH)_2 nanosheets growing on the KNbO_3 perovskite based on electronic structure modulation for enhanced peroxymonosulfate activation, *Environ. Sci. Technol.* 56 (2022) 5200–5212.

[28] X. Zhao, X. Li, Z. Zhu, W. Hu, H. Zhang, J. Xu, X. Hu, Y. Zhou, M. Xu, H. Zhang, G. Hu, Single-atom Co embedded in BCN matrix to achieve 100% conversion of peroxymonosulfate into singlet oxygen, *Appl. Catal. B Environ.* 300 (2022), 120759.

[29] N. Zhang, C. Wang, J. Chen, C. Hu, J. Ma, X. Deng, B. Qiu, L. Cai, Y. Xiong, Y. Chai, Metal substitution steering electron correlations in pyrochlore ruthenates for efficient acidic water oxidation, *ACS Nano* 15 (2021) 8537–8548.

[30] X. Zhang, Y. Ding, H. Tang, X. Han, L. Zhu, N. Wang, Degradation of bisphenol A by hydrogen peroxide activated with CuFe_2O_4 microparticles as a heterogeneous Fenton-like catalyst: Efficiency, stability and mechanism, *Chem. Eng. J.* 236 (2014) 251–262.

[31] G. Yang, Y. Jiao, H. Yan, Y. Xie, A. Wu, X. Dong, D. Guo, C. Tian, H. Fu, Interfacial engineering of $\text{MoO}_2\text{-FeP}$ heterojunction for highly efficient hydrogen evolution coupled with biomass electrooxidation, *Adv. Mater.* 32 (2020) 2000455.

[32] L. Zhou, X. Yang, Y. Ji, J. Wei, Sulfate radical-based oxidation of the antibiotics sulfamethoxazole, sulfisoxazole, sulfathiazole, and sulfamethizole: The role of five-membered heterocyclic rings, *Sci. Total Environ.* 692 (2019) 201–208.

[33] Z. He, H. Wang, M. Li, L. Feng, J. Niu, Z. Li, X. Jia, G. Hu, Amorphous cobalt oxide decorated halloysite nanotubes for efficient sulfamethoxazole degradation activated by peroxymonosulfate, *J. Colloid Interface Sci.* 607 (2022) 857–868.

[34] H. Eibenberger, S. Steenken, P. O'Neill, D. Schulze-Frohlinde, Pulse radiolysis and electron spin resonance studies concerning the reaction of SO_4cdot with alcohols and ethers in aqueous solution, *J. Phys. Chem.* 82 (1978) 749–750.

[35] W. Liu, Z. Ai, M. Cao, L. Zhang, Ferrous ions promoted aerobic simazine degradation with $\text{Fe@Fe}_2\text{O}_3$ core–shell nanowires, *Appl. Catal. B: Environ.* 150 (2015) 1–11.

[36] R. Luo, M. Li, C. Wang, M. Zhang, M.A. Nasir Khan, X. Sun, J. Shen, W. Han, L. Wang, J. Li, Singlet oxygen-dominated non-radical oxidation process for efficient degradation of bisphenol A under high salinity condition, *Water Res.* 148 (2019) 416–424.

[37] Y. Feng, D. Wu, Y. Deng, T. Zhang, K. Shih, Sulfate radical-mediated degradation of sulfadiazine by CuFe_2O_4 rhombohedral crystal-catalyzed peroxymonosulfate: synergistic effects and mechanisms, *Environ. Sci. Technol.* 50 (2016) 3119–3127.

[38] Y. Xu, J. Ai, H. Zhang, The mechanism of degradation of bisphenol A using the magnetically separable CuFe_2O_4 /peroxymonosulfate heterogeneous oxidation process, *J. Hazard. Mater.* 309 (2016) 87–96.

[39] J. Hu, Y. Li, Y. Zou, L. Lin, B. Li, X.-y. Li, Transition metal single-atom embedded on N-doped carbon as a catalyst for peroxymonosulfate activation: A DFT study, *Chem. Eng. J.* 437 (2022), 135428.

[40] Z. Dai, D. Li, Z. Ao, S. Wang, T. An, Theoretical exploration of VOCs removal mechanism by carbon nanotubes through persulfate-based advanced oxidation processes: adsorption and catalytic oxidation, *J. Hazard. Mater.* 405 (2021), 124684.

[41] Y. Chen, G. Zhang, H. Liu, J. Qu, Confining free radicals in close vicinity to contaminants enables ultrafast fenton-like processes in the interspacing of MoS_2 , *Membr., Angew. Chem. Int. Ed.* 58 (2019) 8134–8138.

[42] J. Jing, M.N. Pervez, P. Sun, C. Cao, B. Li, V. Naddeo, W. Jin, Y. Zhao, Highly efficient removal of bisphenol A by a novel Co-doped LaFeO_3 perovskite/PMS system in salinity water, *Sci. Total Environ.* 801 (2021), 149490.

[43] H. Xu, Y. Zhang, J. Li, Q. Hao, X. Li, F. Liu, Heterogeneous activation of peroxymonosulfate by a biochar-supported Co_3O_4 composite for efficient degradation of chloramphenicol, *Environ. Pollut.* 257 (2020), 113610.

[44] M. Zhu, J. Miao, D. Guan, Y. Zhong, R. Ran, S. Wang, W. Zhou, Z. Shao, Efficient wastewater remediation enabled by self-assembled perovskite oxide heterostructures with multiple reaction pathways, *ACS Sustain. Chem. Eng.* 8 (2020) 6033–6042.

[45] Y. Ren, L. Lin, J. Ma, J. Yang, J. Feng, Z. Fan, Sulfate radicals induced from peroxymonosulfate by magnetic ferrospinel MFe_2O_4 (M=Co, Cu, Mn, and Zn) as heterogeneous catalysts in the water, *Appl. Catal. B: Environ.* 165 (2015) 572–578.

[46] W. Liu, Y. Li, F. Liu, W. Jiang, D. Zhang, J. Liang, Visible-light-driven photocatalytic degradation of diclofenac by carbon quantum dots modified porous g-C₃N₄: Mechanisms, degradation pathway and DFT calculation, *Water Res.* 151 (2019) 8–19.

[47] M.J. García-Galán, M. Silvia Díaz-Cruz, D. Barceló, Identification and determination of metabolites and degradation products of sulfonamide antibiotics, *TrAC, Trends Anal. Chem.* 27 (2008) 1008–1022.

[48] W.-D. Oh, A. Veksha, X. Chen, R. Adnan, J.-W. Lim, K.-H. Leong, T.-T. Lim, Catalytically active nitrogen-doped porous carbon derived from biowastes for organics removal via peroxymonosulfate activation, *Chem. Eng. J.* 374 (2019) 947–957.

[49] B. Gao, S. Zhu, J. Gu, Y. Liu, X. Yi, H. Zhou, Superoxide radical mediated Mn(III) formation is the key process in the activation of peroxymonosulfate (PMS) by Mn-incorporated bacterial-derived biochar, *J. Hazard. Mater.* 431 (2022), 128549.

[50] Y. Deng, Z. Zhou, H. Zeng, R. Tang, L. Li, J. Wang, C. Feng, D. Gong, L. Tang, Y. Huang, Phosphorus and potassium Co-doped g-C₃N₄ with multiple-locus synergies to degrade atrazine: Insights into the depth analysis of the generation and role of singlet oxygen, *Appl. Catal. B Environ.* 320 (2023), 121942.